Combustion characteristics of iron-air suspensions: reaction zone structures and reaction front speed

D. Braig[1], M. A. Fedoryk[2], J. Mich[1], S. R. Harth[2], B. Stelzner[2],
A. Scholtissek[1,*], D. Trimis[2] and C. Hasse[1]

*scholtissek@stfs.tu-darmstadt.de

[1] *Technical University of Darmstadt, Department of Mechanical Engineering, Simulation of reactive Thermo-Fluid Systems, Otto-Berndt-Straße 2, 64287 Darmstadt, Germany*
[2] *Engler-Bunte-Institute, Division of Combustion Technology, Karlsruhe Institute of Technology, Engler-Bunte-Ring 7, 76131, Karlsruhe, Germany*

Abstract

Limiting global warming requires a transformation of the energy sector, hence energy generation and storage must become carbon-free and renewable. To replace secured-capacity of conventional power plants, long-term and largescale energy storage together with suitable power supply systems are needed. Metal fuels, especially iron, are promising chemical energy carriers for solving this problem. Similar to other solid fuels, the heat released from the oxidation of iron powder in air can be used for power generation. The products of this process, i. e. iron oxide particles, can subsequently be collected and recycled by means of thermochemical reduction with green hydrogen. This redox cycle holds great potential for a clean circular energy economy. Nevertheless, harnessing the energy stored in iron requires a better understanding of the peculiar physical processes occurring during the reaction of iron-air suspensions. Numerical simulations of iron dust flames, validated against laboratory-scale experiments, can provide fundamental insights into the underlying processes and mechanisms. Since interactions between particles and flow field determine the characteristics of iron-air flames, simulations including particle tracking and a fully-resolved flow field are necessary. In this work, a corresponding simulation of a laminar iron-air Bunsen flame is performed utilizing a multiphase CFD framework based on OpenFOAM®. The iron particles are described by a state-of-the-art single particle model and are tracked by means of a Lagrangian approach while the gas phase is treated as a Eulerian phase. The particle model accounts for the formation of FeO and includes the melting and solidification of iron and FeO. The reaction can either be diffusion-limited or kinetically limited. Furthermore, mass, momentum and conductive heat transfer between the gas phase and iron particles are included as well as radiative heat loss to the environment. The aim of this work is to understand the influence of single-particle modeling on the multi-dimensional iron dust flame, with a particular focus on the reaction zone structure. Therefore, the availability of oxygen in the vicinity of the reaction zone are investigated. Furthermore, the influences of particle and flow properties are determined, examining particle trajectories and velocities. The results are compared to recent experimental data and serve as a reference case for developing a better understanding of iron-air flames.

1 Introduction

Reducing greenhouse gas emissions from the energy sector, governments worldwide are confronted with the challenge of balancing intermittent energy production from the growing renewable energy sector with sustaining grid stability and power supply at large scales. To this end, chemical energy carriers, synthesized using renewable energy sources, can serve to transfer energy from regions with high potential for renewables to densely populated or industrial regions with high energy demand. An interesting category of carbon-free energy carriers, which have received increased attention lately, are metals. As proposed by Bergthorson [1], metal and metal oxide powders can be used to operate a carbon-free energy cycle in which the metal oxides are reduced with green hydrogen (energy storage) and the metals are then oxidized (energy release) at a different location and at a different time. A promising candidate for constructing such a metal-based energy cycle is iron, which is in the focus of this work. Compared to other solid fuels, like coal and biomass, research on iron powders for energy storage and

supply is still in its infancy, even though early experimental works date back more than two decades [2], [3]. A lot of the pioneering work on iron (and other metal fuels for heat and power supply) has been performed at McGill University in Canada by Goroshin, Bergthorson and co-workers [4], [5]. In the last few years, further research projects focusing on metal fuels and particularly iron have emerged also throughout Europe and in China.

To release energy from iron powder, the material can be rapidly oxidized with air in iron dust flames releasing the stored energy as heat. However, the operation of iron dust flames is non-trivial since there exist several fundamental differences between such (non-volatile) solid fuel flames and conventional gas flames as pointed out by Goroshin et al. [5]: the solid material can significantly exceed the gas temperature, fuel concentration and temperature profiles differ since the fuel (i.e. the iron particles) does not diffuse, and the flame structure becomes distorted due to thermal inertia and phase transitions of the solid material. In consequence, the flame's speed and temperature show different responses to fuel-oxygen equivalence ratio as compared to gas flames [5]. In the past, iron dust flames have been established experimentally in different configurations, such as counterflow flames [6] Bunsen-type flames [7] or top-fired swirled tornado flames [8]. Even though several stable flames could be operated in the lab, important flame characteristics such as the flame stabilization mechanisms are not thoroughly understood and warrant further research. This represents the motivation of our present study.

The objective of this work is the development of a numerical model for the self-sustained iron-air Bunsen flame which has been investigated at KIT [9]. The model is used to analyze the flame anchoring mechanism, the flame structure and the dynamics between flow, flame, and the polydisperse iron microparticles. With this, the current work contributes to our understanding of iron dust flames and shall help to operate iron dust flames in a reliable manner in future applications.

2   Experimental Bunsen flame setup

The experimental setup utilizes iron powder of >99.5% purity (PMCtec GmbH, type YTF-HY2) as a fuel, which is contained in a cylindrical tube and shifted upwards by a piston connected to a stepper motor as shown in Figure 1. The dispersion of the iron powder occurs in a so-called air-knife seeder in a small gap of approx. 30 µm height with high gas velocity. The air mass flow in the seeder/burner and co-flow stream is controlled by mass flow controllers.
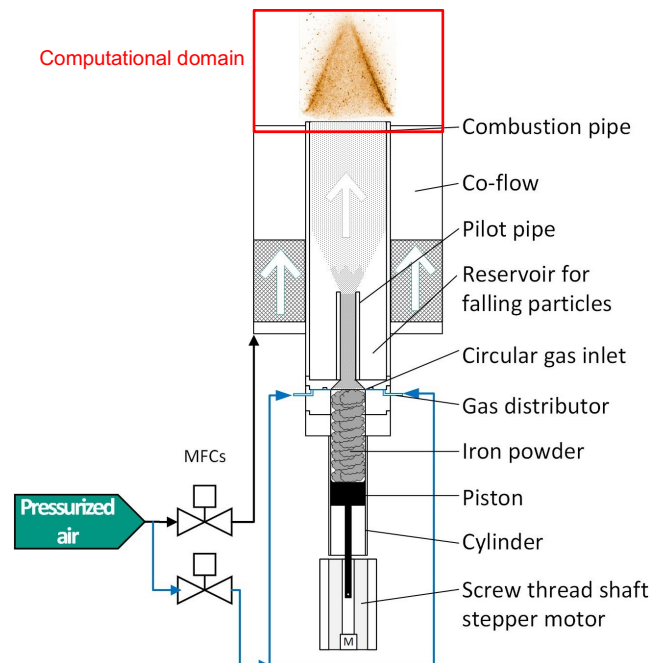

Figure 1 – Schematic of the experimental setup. The computational domain is marked by a red box.

Figure 1 further shows the burner setup which consists of two concentric tubes: an inner pilot tube and an outer combustion tube of the diameter of 20.5 mm and of the length of 35 cm downstream from the pilot tube outlet. As the iron powder suspension exits the pilot tube, the flow slows down, causing some

of the (bigger) particles to fall down and it has been observed that few particles can also stick to the wall of the larger combustion tube. The falling powder is collected in a separate container, minimizing fluctuations for the seeding process. The length of the pilot tube is adjusted to provide sufficient space for the falling powder. The outlet tube of the burner is surrounded by a co-flow with a larger diameter to enhance flame stability and protect the flame from external influences. Both, the co-flow and combustion air, were supplied at room temperature. A more detailed description can be found in [9].

3   Numerical methods

In the following, we present the framework for the numerical simulations of the iron-air Bunsen flame including the governing equations for gas and particulate phases as well as the relevant boundary conditions. Thereafter, details about the computational setup are provided.

3.1   Euler-Lagrange framework

The iron-air Bunsen flame is simulated with an OpenFOAM®-based CFD code utilizing the Euler-Lagrange framework. Iron microparticles are modeled as point particles according to the particle source in cell approach. The usual governing equations for mass, momentum, enthalpy, and chemical species read:

$$\frac{\partial \rho}{\partial t} + \frac{\partial (\rho u_i)}{\partial x_i} = S_{\mathrm{prt},m} \,,$$

(1)

$$\frac{\partial (\rho u_i)}{\partial t} + \frac{\partial (\rho u_i u_j)}{\partial x_j} = -\frac{\partial p}{\partial x_i} - \frac{\partial \tau_{ji}}{\partial x_j} + \rho g_i + S_{\mathrm{prt},u_i} \,,$$

(2)

$$\frac{\partial (\rho h)}{\partial t} + \frac{\partial (\rho u_j h)}{\partial x_j} = \rho u_j g_j - \frac{\partial q_j}{\partial x_j} + S_{\mathrm{prt},h} \,,$$

(3)

$$\frac{\partial (\rho Y_i)}{\partial t} + \frac{\partial (\rho u_j Y_i)}{\partial x_j} = \frac{\partial}{\partial x_j}\left(\rho D_i \frac{\partial Y_i}{\partial x_j} \right) + S_{\mathrm{prt},Y_i} \,,$$

(4)

where ρ is the density, u_i is the flow velocity in spatial dimension x_i, p is the pressure, τ_{ij} is the stress tensor, g_i is the gravity in spatial dimension x_i, h is the enthalpy, q_i is the heat flux in spatial dimension x_i , Y_i is the mass fraction and D_i is the diffusivity of species i. Further, in the above set of equations $S_{()}$ represent exchange terms between the continuous gas and the disperse solid phase. These terms are defined together with the governing equations for the disperse iron phase in the next subsection.

3.2   Particle model: First Order Surface Kinetics (FOSK) model

We use a particle model based on the work of Soo et al. [10], [11] which has been applied to one-dimensional polydisperse iron-air flames by Mich et al. [12]. Here, the framework by Mich et al. [12] is adapted for OpenFOAM®. The particle model describes the thermochemical oxidation rate of the iron particles by either First Order Surface Kinetics, FOSK (kinetically-controlled regime) or by the semi-empirical Ranz-Marshall correlation [13] for the boundary layer diffusion of oxygen (diffusion-limited regime). The evolution of the particle state is described by the following equations:

$$\frac{\mathrm{d}m_p}{\mathrm{d}t} = \dot{m}_{O_2,\mathrm{kin}} = \dot{m}_{O_2,\mathrm{diff}} \,,$$

(5)

$$\dot{m}_{O_2,\mathrm{kin}} = Y_{O_2,s} A_p k_\infty \exp\left(\frac{-T_a}{T_p} \right),$$

(6)

$$\dot{m}_{O_2,\mathrm{diff}} = \rho_f A_p \frac{\mathrm{Sh} D_{O_2,f}}{d_p} (Y_{O_2,g} - Y_{O_2,s})$$

(7)

$$\frac{\mathrm{d}H_p}{\mathrm{d}t} = \dot{q}_{\mathrm{conv}} + \dot{q}_{\mathrm{rad}} + \frac{\mathrm{d}m_p}{\mathrm{d}t} h_{O_2,s},$$

(8)

$$m\frac{\mathrm{d}u_i}{\mathrm{d}t} = mg_i + F_{d,i} \tag{9}$$

$$F_{d,i} = \frac{1}{2}\rho_c|u_{c,i} - u_{p,i}|(u_{c,i} - u_{p,i})C_d A \tag{10}$$

$$C_d = \frac{24}{\mathrm{Re}_{p,i}}(1 + \frac{1}{6}\mathrm{Re}_{p,i}^{2/3}) \tag{11}$$

where $\mathrm{d}m_p/\mathrm{d}t$ the change of particle mass, $\dot{m}_{O_2,\mathrm{kin}}$ is the change in oxygen based on the particle kinetics, $\dot{m}_{O_2,\mathrm{diff}}$ is the maximum diffusion rate of oxygen from the bulk to the surface of the particle, A_p is the surface area of the particle, k_∞ is the pre exponential factor, T_a is the activation temperature, T_p is the particle temperature, Sh is the Sherwood number, d_p is the particle diameter, $\mathrm{d}H_p/\mathrm{d}t$ is the change of particle enthalpy, $\mathrm{d}u_i/\mathrm{d}t$ is the change of the particle velocity in spatial dimension x_i, $F_{d,i}$ is the drag force in spatial dimension x_i, A is the cross-sectional area and Rep is the particle Reynolds number.

As stated earlier, the particle's oxidation rate in Eq. (5) can be either limited by the kinetic rate ($\dot{m}_{O_2,\mathrm{kin}}$), or the diffusion rate ($\dot{m}_{O_2,\mathrm{diff}}$), which also determines the oxygen concentration at the particle surface, $Y_{O_2,s}$. The latter represents an eigenvalue of the problem and approaches zero in the diffusion limited case and the oxygen mass fraction in the bulk in the kinetically controlled regime. Further, the particle thermodynamics (phase densities, heat capacities, etc.) are described with correlations from the NIST database [14], including transitions between phases. Further information on the particle model is provided in [12].

Based on Eqs. (5)-(11), the exchange terms with the gas phase are defined as:

$$S_{\mathrm{prt},m} = \frac{1}{V_{cell}}\sum_k -\frac{\mathrm{d}m_p}{\mathrm{d}t}n, \tag{12}$$

$$S_{\mathrm{prt},u_i} = \frac{1}{V_{cell}}\sum_k -F_{d,i}n, \tag{13}$$

$$S_{\mathrm{prt},h} = \frac{1}{V_{cell}}\sum_k -(\dot{q}_{\mathrm{conv}} + \frac{\mathrm{d}m_p}{\mathrm{d}t}h_{O_2,s})n, \tag{14}$$

$$S_{\mathrm{prt},Y_{O_2}} = \frac{1}{V_{cell}}\sum_k -\frac{\mathrm{d}m_p}{\mathrm{d}t}n, \tag{15}$$

where V_{cell} is the volume of the corresponding cell, the subscript k represents the parcels per cell and n the number of particles per parcel. Notably, the positioning of a particle within a cell of the computational domain can alter the particle boundary conditions, especially when encountering high gradients in the gas phase. Therefore, the relevant gas phase conditions (e.g. bulk temperature, oxygen concentration) are interpolated between different cells to the individual particle position. The computational overhead by this measure is overcompensated by improvements in solver stability and the possibility to use a coarser mesh.

3.3 Numerical setup

The three-dimensional computational domain for the Bunsen flame is indicated in Figure 1. It is discretized with 160.512 cells with inlets for the main pipe flow (particles+air) and co-flow (air) at the bottom of the domain and outlet conditions at the top and the sides of the domain. The pipe is described as a no-slip wall. An overview of the boundary conditions is provided in Table 1.

Table 1 – Boundary conditions specified for the computational domain.

Surface	BC: T	BC: U	BC: p
Combustion pipe	fixed value 323K	fixed value (Exp. data)	zero gradient
Co-flow	fixed value (298K)	fixed value (25cm/s)	zero gradient
Wall	zero gradient	no slip	zero gradient
Surroundings	zero gradient	inlet/outlet (no back flow)	wave transmissive (1 atm)

Parcels are seeded in the main flow according to the particle size distribution specified by Fedoryk et al. [9] with one parcel representing between 1 particle (medium-large particles) up to 290 particles (smallest particle fraction). In total, approximately 150,000 particles need to be transported within the computational domain with most of the parcels located in the lower part of the domain, before they are accelerated towards the outlet when passing the flame front. The particle velocities at the inlet are determined from the measured gas velocity profile and the sinking velocity determined from the particles' size and density (see Figure 2, left). Due to gravitational forces and locally varying gas velocity within the pipe, bigger particles cannot be carried by the flow near the pipe walls and a radial variation in particle loading and size distribution develops inside of the pipe. Therefore, the particle's sinking velocity is treated as a slip velocity between gas phase and individual particle, such that the seeding velocity for each particle size fraction is determined according to $u_0(d_p) = u_{\text{gas}} - u_{\text{slip}}(d_p)$. If a particle's velocity formally becomes negative because the slip velocity exceeds the local gas velocity, it is not seeded and discarded. This way, smaller particles, which readily follow the flow, are distributed across the full nozzle diameter, while larger particles only occur in the center of the pipe flow (see Figure 2, right). A simulation of a fully developed pipe flow and its influence on the local flame conditions as well as the overall flame stability are a subject for future work.

The flame is initiated by a three-step process: (1) a cold particle-laden jet is simulated first, (2) thereafter, particles are ignited by imposing a "hot ring" at the pipe outlet until a flame has developed, and (3) the hot ring is deactivated and the simulation is continued until a statistically steady flame has developed.
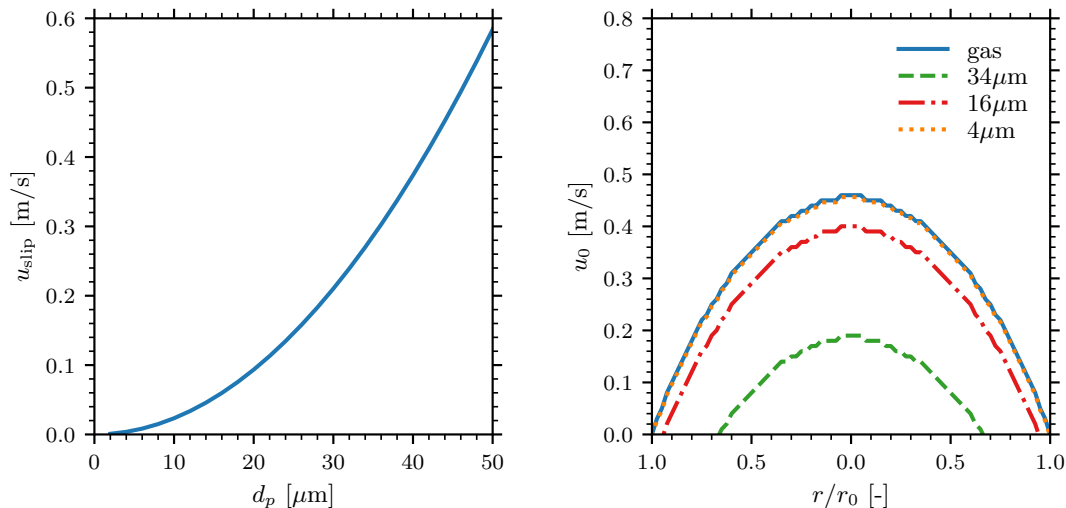

Figure 2 – Left: sinking velocity as a function of particle diameter, which is treated as the slip velocity between gas phase and individual particle size fractions. Right: bigger particles have lower seeding velocities and preferentially occur in the middle of the pipe flow, while smaller particles can readily follow the flow and are seeded across the whole nozzle diameter.

4   Results and discussion

In this section, the simulation results are first visually compared to the experimental flame images. Thereafter, the overall flame characteristics are analyzed and discussed in relation to the experimental findings. Lastly, special attention is put on the dynamics and particle distribution inside the flame.

4.1   Comparison with experimental flame images

Figure 3 shows the instantaneous flame image generated from the simulation of the self-sustained Bunsen flame (left) together with corresponding images recorded from the experiments by Fedoryk et al. [9] (right). For the simulation results, the particles are scaled according to their size and the non-dimensionalized temperature is treated as an intensity signal (non-dimensionalization between 1300K and $T_{max} \approx 2800$ K). The flame exhibits a conical shape which resembles the flame in the experiments. Differences in the visual appearance in Figure 3 stem from the fact that the intensity for the smallest particles is vastly under resolved in the simulation (290 particles are represented by one parcel for the smallest particle size) which otherwise appear as a "white dust curtain" in the experimental single shot image and also lead to a visually well-defined flame front. Contrary, the image from the simulation predominantly shows the larger particles. It is further found that the flame height is overpredicted in the
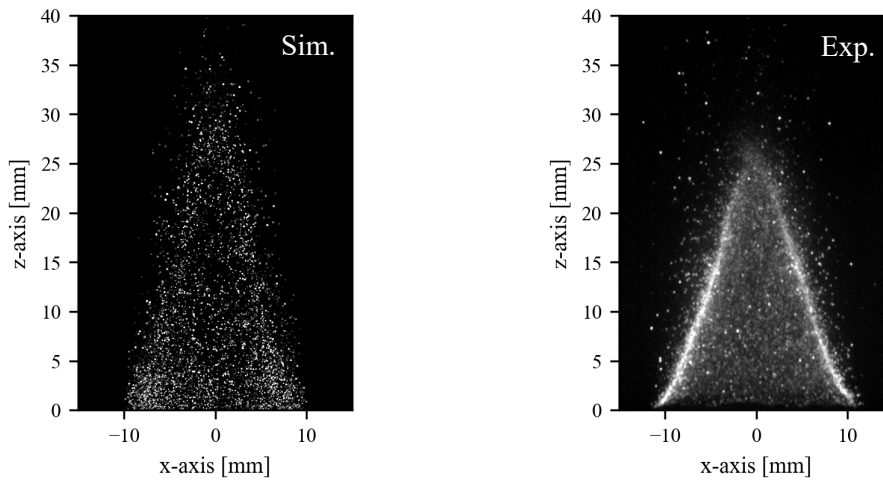

Figure 3 – Line of sight flame images obtained from the simulations (left) and the experiments of an iron-air flame at equivalence ratio Φ_{Fe2O3}=1 and average gas inlet velocity of 25 cm/s (right).

simulation, an aspect which we found to be sensitive when varying the inlet conditions, such as particle size distribution and initial temperature (not shown here). There are three primary reasons which serve as explanations for the differences: First, it is to be expected that a fully developed flow inside of the main pipe will impact the particle distribution at the pipe outlet and differ from the currently imposed particle boundary conditions. Second, there still exists a significant uncertainty regarding the ignition behavior of iron microparticles [15][16] which is strongly correlated with the local flame speed [17] and therefore the flame height and cone angle. Third, the current model does not account for particle-particle radiation, which has yet to be integrated and its impact on the flame physics needs to be assessed. We note, however, that particle-particle radiation should play a secondary role according to experiments [5]

4.2   Overall flame characteristics

The simulation results offer detailed insights into the flame configuration which we analyze next. Figure 4 visualizes the iron-air flame showing both temperature (top) and oxygen mass fraction fields (bottom) together with the iron microparticles. The simulations are run for two seconds physical time and during this time span the flame was self-sustained showing slight lateral movements close to the flame tip. Overall, the flame front appears continuous but exhibits slight discrete effects, which can again be attributed to the high amount of particles per parcel for smaller particle size fractions.

Inspecting Figure 4 (top), elevated gas phase temperatures are found at the flame base and around the tip with few large hot particles (colored dark grey to black) above the flame front. It is generally observed that the particle spacing declines after the flame front, which is to be expected due to thermal

6

expansion and increased flow velocities. In the shear layer between the hot exhaust gases and the co-flow smaller particles appear to cool down and accumulate (bright colors). Interestingly, the flame stabilizes close to the inlet indicating a propensity for flashback in the current configuration.

The oxygen distribution in Figure 4 shows a depletion of oxygen after the flame front (dark to bright blue) and the particle oxidation proceeds in a similar manner, since iron is consumed for most particles shortly after passing the flame front. Overall, the equivalence ratio is chosen as one for the present case, which however refers to the oxidation to Fe2O3. Keeping in mind that the model only considers oxidation to FeO (which only amounts to 66% of the full oxidation state) it is conceivable that excess oxygen remains after the flame front and the majority of particles burns in a lean environment. Opposite to the rest of the domain, a depletion of oxygen to almost zero can be observed at the flame base which is likely due to the low flow velocities and local rich mixture close to the nozzle walls. Similarly, when comparing the flame tip to the flame flank, a slight oxygen depletion can be observed. This effect can be attributed to the particle dynamics, which are examined in the next subsection.
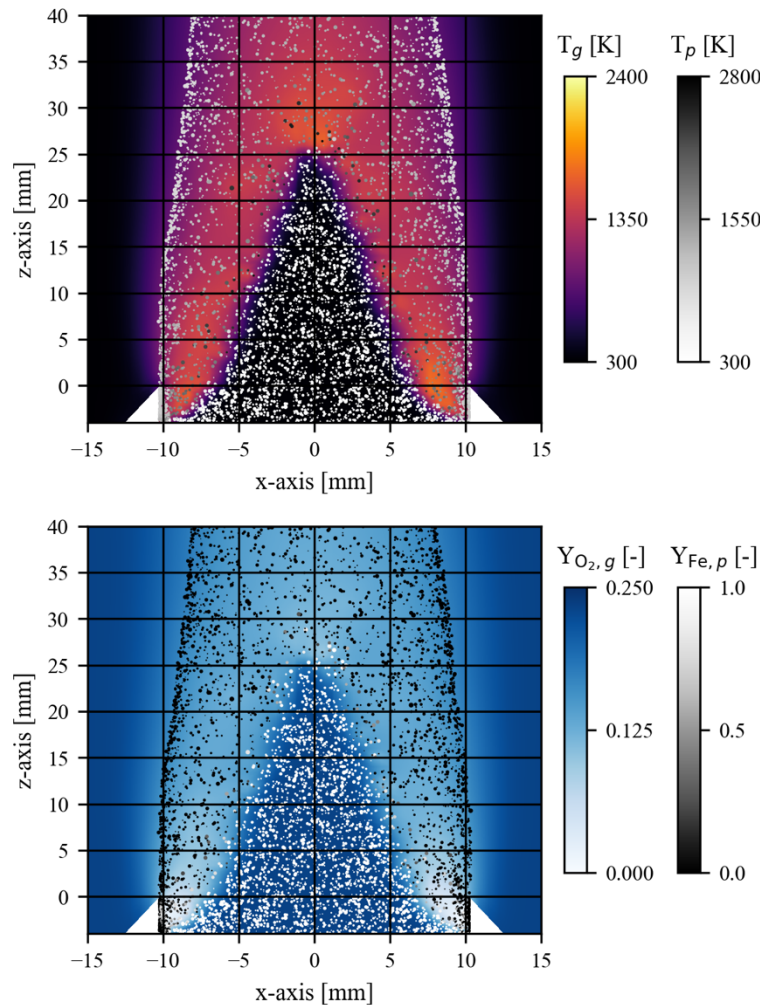

Figure 4 – Instantaneous snapshots of gas and particle temperatures (top) as well as the oxygen mass fraction in the gas phase (bottom) with a superposition of the microparticles colored according to their conversion (as indicated by the iron content).

4.3 Particle dynamics

In order to investigate the particle dynamics in the iron-air flame, we proceed by tracking particles of different size fractions as they pass the flame front. To this end, the path of the particles through the iron-air flame can be visualized as a particle trajectory. In Figure 5, the trajectories for small ($d_p = 4$ μm, left) and large ($d_p = 34$ μm, right) particles are shown. As stated earlier, smaller particles are found across the full nozzle diameter, which is also indicated by the trajectories, while larger particles are can

only follow the flow in the middle of the pipe flow. Generally, the particle trajectories indicate movement of the particles towards the flame front due to thermal expansion and the associated acceleration of the particles along the flame-normal direction. Interestingly, bigger particles at the sides seem to get slightly deflected at first from the flame base before passing the flame front. For smaller particles, the trajectories passing through the flame base region approach each other downstream, which matches with the observation of preferred particle accumulation in the shear layer between exhaust gases and co-flow. This can be explained by the flame curvature at the flame base which directs multiple particle trajectories towards each other.
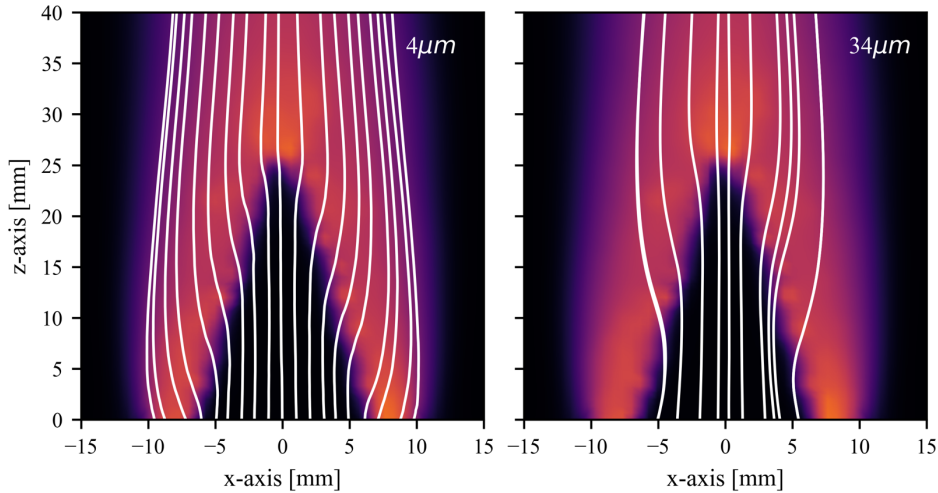

Figure 5 – Particle trajectories for small ($d_p = 4$ µm, left) and large particles ($d_p = 34$ µm, right). The colored contours in the background correspond to the temperature field also shown in Figure 4 (top).

5 Conclusion and outlook

In this work we present a first simulation of the iron-air Bunsen flame experiments carried out by Fedoryk et al. [9]. Overall, the simulated flame shows qualitative similarities to the experiments but still deviates quantitatively in key observables such as the flame height and the cone angle. Similar as in the experiments, the iron-air flame is self-sufficient in the simulation and does not require support through additional combustible gaseous fuels in the inlet stream. The flame appears continuous and quasi-stationary with slight lateral movements at the flame tip. The numerical results further illustrate how the flame characteristics depend on the particle boundary conditions at the nozzle inlet which persist throughout the flame and the post-flame region. In future work, the particle dynamics inside of the nozzle will be simulated to resolve the effect of the radially varying particle loading and size distribution on the flame stabilization mechanism and its overall structure. Besides this, there still remain uncertainties in the particle modeling (ignition temperatures, flame speeds) which are expected to influence the flame topology and also warrant further research.

References
[1]   J. M. Bergthorson, "Recyclable metal fuels for clean and compact zero-carbon power," *Prog. Energy Combust. Sci.*, vol. 68, pp. 169–196, Sep. 2018.
[2]   S. Goroshin, M. Kolbe, J. Bellerose, and J. Lee, "Microgravity Apparatus and Ground-Based Study of the Flame Propagation and Quenching in Metal Dust Suspensions.," *Seventh Int. Workshop Microgravity Combust. Chem. React. Syst.*, Aug. 2003.

[3] F.-D. Tang, S. Goroshin, A. Higgins, and J. Lee, "Flame propagation and quenching in iron dust clouds," *Proc. Combust. Inst.*, vol. 32, no. 2, pp. 1905–1912, 2009.

[4] J. M. Bergthorson *et al.*, "Direct combustion of recyclable metal fuels for zero-carbon heat and power," *Appl. Energy*, vol. 160, pp. 368–382, Dec. 2015.

[5] S. Goroshin, J. Palečka, and J. M. Bergthorson, "Some fundamental aspects of laminar flames in nonvolatile solid fuel suspensions," *Prog. Energy Combust. Sci.*, vol. 91, p. 100994, Jul. 2022.

[6] M. McRae, P. Julien, S. Salvo, S. Goroshin, D. L. Frost, and J. M. Bergthorson, "Stabilized, flat iron flames on a hot counterflow burner," *Proc. Combust. Inst.*, vol. 37, no. 3, pp. 3185–3191, 2019.

[7] P. Julien, S. Whiteley, S. Goroshin, M. J. Soo, D. L. Frost, and J. M. Bergthorson, "Flame structure and particle-combustion regimes in premixed methane–iron–air suspensions," *Proc. Combust. Inst.*, vol. 35, no. 2, pp. 2431–2438, 2015.

[8] M. Baigmohammadi, W. Prasidha, N. C. Stevens, Y. L. Shoshyn, T. Spee, and P. De Goey, "Towards utilization of iron powders for heating and power," *Appl. Energy Combust. Sci.*, vol. 13, p. 100116, Mar. 2023.

[9] M. Fedoryk, B. Stelzner, S. Harth, and D. Trimis, "Experimental investigation of the laminar burning velocity of iron-air flames in a tube burner," *Appl. Energy Combust. Sci.*, vol. 13, p. 100111, Mar. 2023.

[10] M. Soo, S. Goroshin, J. M. Bergthorson, and D. L. Frost, "Reaction of a Particle Suspension in a Rapidly-Heated Oxidizing Gas," *Propellants Explos. Pyrotech.*, vol. 40, no. 4, pp. 604–612, Aug. 2015.

[11] M. J. Soo, K. Kumashiro, S. Goroshin, D. L. Frost, and J. M. Bergthorson, "Thermal structure and burning velocity of flames in non-volatile fuel suspensions," *Proc. Combust. Inst.*, vol. 36, no. 2, pp. 2351–2358, 2017.

[12] J. Mich, D. Braig, T. Gustmann, C. Hasse, and A. Scholtissek, "A comparison of mechanistic models for the combustion of iron microparticles and their application to polydisperse iron-air suspensions." arXiv, Jun. 13, 2023. Accessed: Jun. 30, 2023. [Online]. Available: http://arxiv.org/abs/2304.14927

[13] W. E. Ranz, "Evaporation from drops," *Chem. Eng. Prog.*, vol. 48, pp. 142–180, 1952.

[14] M. W. Jr. Chase, "NIST-JANAF themochemical tables, fourth edition," *J. Phys. Chem. Ref. Data*, vol. 9, pp. 1–1951, 1998.

[15] X. Mi, A. Fujinawa, and J. M. Bergthorson, "A Quantitative Analysis of the Ignition Characteristics of Fine Iron Particles," *Combust. Flame*, vol. 240, p. 112011, Jun. 2022.

[16] T. Hazenberg and J. A. Van Oijen, "Structures and burning velocities of flames in iron aerosols," *Proc. Combust. Inst.*, vol. 38, no. 3, pp. 4383–4390, 2021.

[17] S. Goroshin, F.-D. Tang, and A. J. Higgins, "Reaction-diffusion fronts in media with spatially discrete sources," *Phys. Rev. E*, vol. 84, no. 2, p. 027301, Aug. 2011.